Power Electronics and Applications (EPE'17 ECCE-Europe), 2017 19th European Conference on

Thermal Modeling and Experimental Verification of an Air Cooled Medium Frequency Transformer

M. Mogorovic and D. Dujic

POWER ELECTRONICS LABORATORY
ÉCOLE POLYTECHNIQUE FÉDÉRALE DE LAUSANNE

Thermal Modeling and Experimental Verification of an Air Cooled Medium Frequency Transformer

Marko Mogorovic, Drazen Dujic
Power Electronics Laboratory
École Polytechnique Fédérale de Lausanne - EPFL
Station 11, CH-1015 Lausanne
Email: marko.mogorovic@epfl.ch, drazen.dujic@epfl.ch
URL: http://pel.epfl.ch

Keywords

<<Transformer>>, <<Modelling>>, <<Thermal design>>, <<Cooling>>, <<Resonant converter>>

Abstract

This paper provides detailed analytical modeling and finite elements method (FEM) analysis of the thermal behavior of the medium frequency transformer (MFT). A comprehensive analytical model in form of a thermal network consisting of conduction, convection and radiation thermal resistances is generated based on the transformer physical structure, thus allowing for fast optimization of the MFT design in terms of hot-spot temperatures. The derived analytical models are benchmarked and verified against FEM models and measurements obtained from the developed MFT prototype.

Nomenclature

A_p - MFT area product (measure of size)
P_n - MFT nominal power
K_f - Excitation waveform coefficient
K_u - Window utilization coefficient
B_m - Peak flux density
J - Current density
f_s - Switching frequency
$\mathbf{Y_{th}}$ - Thermal network admittance matrix
$\mathbf{\Delta T}$ - Temperature rise vector
$\mathbf{Q}$ - Injected heat power vector

Introduction

Steady advancements of the silicon semiconductor devices traditionally used in high power applications and the proliferation of the wide-band-gap semiconductor devices (e.g. SiC and GaN) are driving the research in directions of novel and ever faster switching galvanically isolated conversion topologies, referred to in literature as power electronic transformers (PETs) [1] or solid state transformers (SSTs) [2]. Generally, SST concepts avoid the use of the bulky line frequency transformers and are characterized with power electronics stages at each of the terminals. Depending on the construction and application, all of these topologies utilize either a single or multiple MFT units to achieve the galvanic isolation and input-output voltage level matching.

Operation of the transformer at the medium frequency, enabled by the fast switching of the power semiconductors, allows for a substantial reduction of the transformer size compared to the traditional line frequency transformers according to the approximate relation (1). Other design variables that have an impact on the MFT size (e.g. insulation, cooling, etc.) are limited by the corresponding material properties and their values cannot be changed in the orders of magnitude as it can be done with frequency. This is especially important for on-board traction applications, where both the weight and volume are paramount design criteria [1].

Fig. 1: Shell MFT geometry

$$A_p \approx \frac{P_n}{K_f K_u B_m J f_s} \tag{1}$$

Nevertheless, this reduction in size of the MFT directly affects the cooling conditions due to the decreased cooling surface, as illustrated in Fig. 1. Decreased cooling surface implies increased thermal resistances towards the ambient (cooling media) which result in higher temperature gradients. Therefore, accurate thermal modeling, that allows for adequate MFT thermal coordination at the design stage, plays an essential role in the search for the overall optimal design [3–7].

This paper provides a detailed FEM thermal analysis, derivation and experimental verification of a comprehensive analytical thermal network model, based on the conduction, convection and radiation thermal resistances, capable of accurately estimating the temperature rise at the hot-spots within the windings and the core in the steady state. This model is suitable for the design optimization purposes due to its simplicity and low computational cost, thus allowing to include the thermal considerations into the overall design optimization procedure. For the purpose of validation, the results of the developed anlytical model are compared with FEM model simulations and measurements obtained from the MFT prototype.

MFT Design Optimization

A brute force MFT design optimization algorithm capable of generating both all mathematically possible and standard-component-based solutions, including dedicated performance filters, presented in [8], is displayed in Fig. 2.

As shown in Fig. 2a, a basic requirement for any design optimization are the models of all the relevant phenomena related either to optimization constraints or objectives allowing the estimation of the same. However, besides the precision and accuracy as main figures of merit of any model, when it comes to modeling for optimization purposes, there exists a third requirement that has a critical effect on the model quality. Namely, regardless of the level of sophistication, all optimization algorithms need to execute all of the associated models numerous times in their search for the optimal solution. Therefore, it is essential that all the modeling is performed with least possible computation effort. Consequently, modeling for design optimization purposes is subject to a trade-off between the precision and accuracy (e.g. FEM

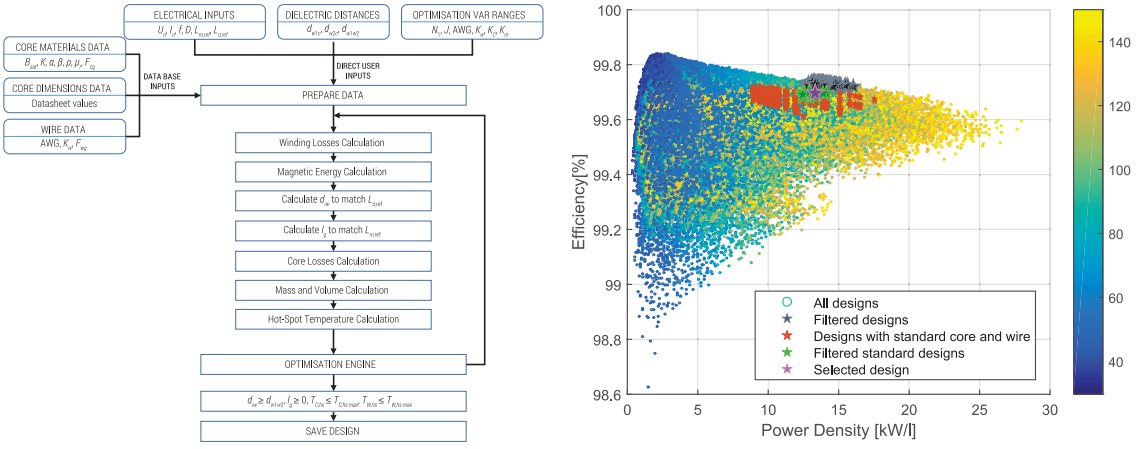

(a) (b)

Fig. 2: (a) MFT design optimization algorithm; (b) Optimization results (around two million designs) plotted as efficiency vs. volumetric power density with color map indicating winding hot-spot temperature determined with analytical model;

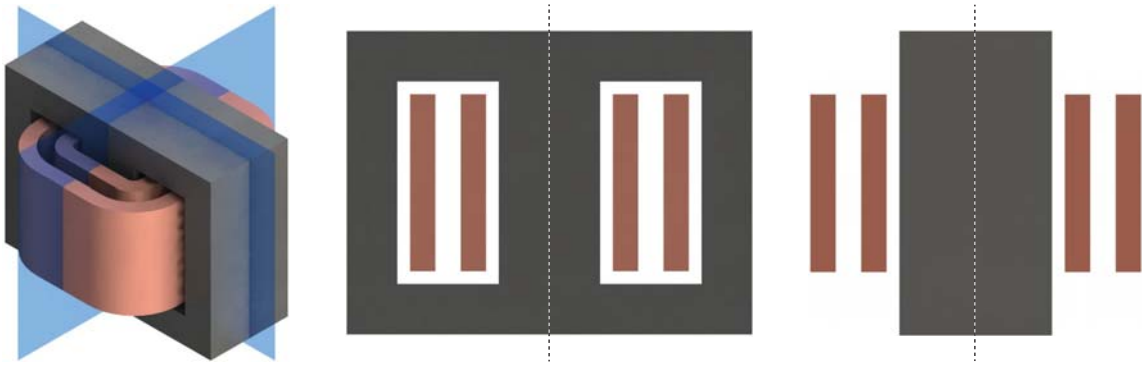

(a) (b) (c)

Fig. 3: (a) 3D MFT structure with highlighted thermal planes of symmetry; (b) 2D symmetry detail capturing the geometry within the core window; (c) 2D symmetry detail capturing the geometry outside of the core window;

models) on the one hand and execution speed (e.g. analytical models) on the other. Finally, the quality of any design optimization boils down to the quality of the utilized models in terms of their precision accuracy and speed. The derivation and verification of a computationally non-intensive and sufficiently accurate and precise analytical thermal MFT model are presented in what follows.

Analytical Thermal Model

Estimation of the MFT hot-spot temperatures is a complex 3D heat transfer problem, as displayed in Fig. 1, which includes all three types of heat transfer mechanisms: conduction, convection and radiation. However, taking into account the symmetry of the MFT geometry, as illustrated in Fig. 3a, it is possible to reduce the 3D heat transfer model to two 2D geometry details, as shown in Figs. 3b and 3c, characterizing the different cooling conditions of the winding portions, inside and outside of the core window.

In addition to this, it is possible to further reduce this model to a single 2D geometry detail, as displayed in Fig. 4a without neglecting the effects of the part of the winding that is outside of the shell core window using an assumption that there is no temperature gradient within the winding in the tangential direction of the wire. This is a reasonable assumption which is very close to reality, due to the high temperature conductance of copper compared to the enamel insulation, which allows to indirectly include the effect of the different cooling conditions of both winding portions, inside and outside of the core window, on the winding hot-spot temperature in a simple manner, by putting in parallel their corresponding heat transfer resistances.

Table I: Empirical heat-transfer formulas for conduction, convection and radiation [3, 9, 10]

Conduction	$Q_h = kA\frac{\Delta T}{L}$			
Convection over Hot-Plate	$Q_h = hA(T_s - T_\infty)$	Top:	$h = \frac{k(0.65+0.36R_{a_L}^{1/6})^2}{L}$	$L = \frac{\text{Area}}{\text{Perimeter}}$
		Side:	$h = \frac{k}{L}\left(0.825 + \frac{0.387R_{a_L}^{1/6}}{\left(1+(0.492/P_r)^{9/16}\right)^{8/27}}\right)^2$	$L = \text{Height}$
		Bottom:	$h = \frac{k0.27R_{a_L}^{1/4}}{L}$	$L = \frac{\text{Area}}{\text{Perimeter}}$
Radiation	$Q_h = hA(T_1 - T_2)$		$h = \epsilon\sigma\frac{(T_1+273.15)^4-(T_2+273.15)^4}{(T_1-T_2)}$	

where: R_{a_L} - Rayleigh number, P_r - Prandtl number, ϵ - Emissivity, σ - Stefan–Boltzmann constant

Table II: Frequency dependent core and winding loss calculation of the injected thermal energy [5, 11, 12]

Core losses	$P_s = 2^{\alpha+\beta} k_i f^{\alpha} B_m^{\beta} D^{1-\alpha}$	$k_i = \dfrac{K}{2^{\beta-1}\pi^{\alpha-1}\left(0.2761 + \frac{1.7061}{\alpha+1.354}\right)}$
Winding losses	$P_\sigma = I^2 \dfrac{mL_w}{\delta\sigma h_w}\left[\dfrac{\sinh(2\Delta')+\sin(2\Delta')}{\cosh(2\Delta')-\cos(2\Delta')} + \dfrac{2}{3}(m^2-1)\dfrac{\sinh(\Delta')-\sin(\Delta')}{\cosh(\Delta')+\cos(\Delta')}\right]$	

where: K, α, β - Steinmetz coefficients, f - Operation frequency, D - Duty-cycle, B_m - Peak magnetic induction, m - Number of equivalent foil winding layers, σ - conductivity, δ - skin depth, Δ' - equivalent penetration ratio

A detailed thermal network consisting of conduction, convection and radiation thermal resistances, as illustrated in Fig. 4b and described by Table I, is generated based on the derived 2D representation, shown in Fig. 4a. This 2D MFT geometry detail can be partitioned into different zones with respect to the occurring physical phenomena, heat transfer and distributed heat injection within the core and winding volume caused by the corresponding losses, as given in Table II.

The core area is divided into four zones corresponding to center and outer limb and top and bottom yoke, as illustrated in Fig. 4a. It is assumed that the core losses are evenly distributed within the core volume. Therefore, the injected heat in each core zone is proportional to its volume in respect to the total core losses. Primary and secondary wingdings are represented with the two corresponding zones. Finally, the thermal network is constructed by taking into account all of the thermal couplings between all of the zones and surrounding air at ambient temperature via conduction, convection and radiation, as shown in Fig. 4b and Table I.

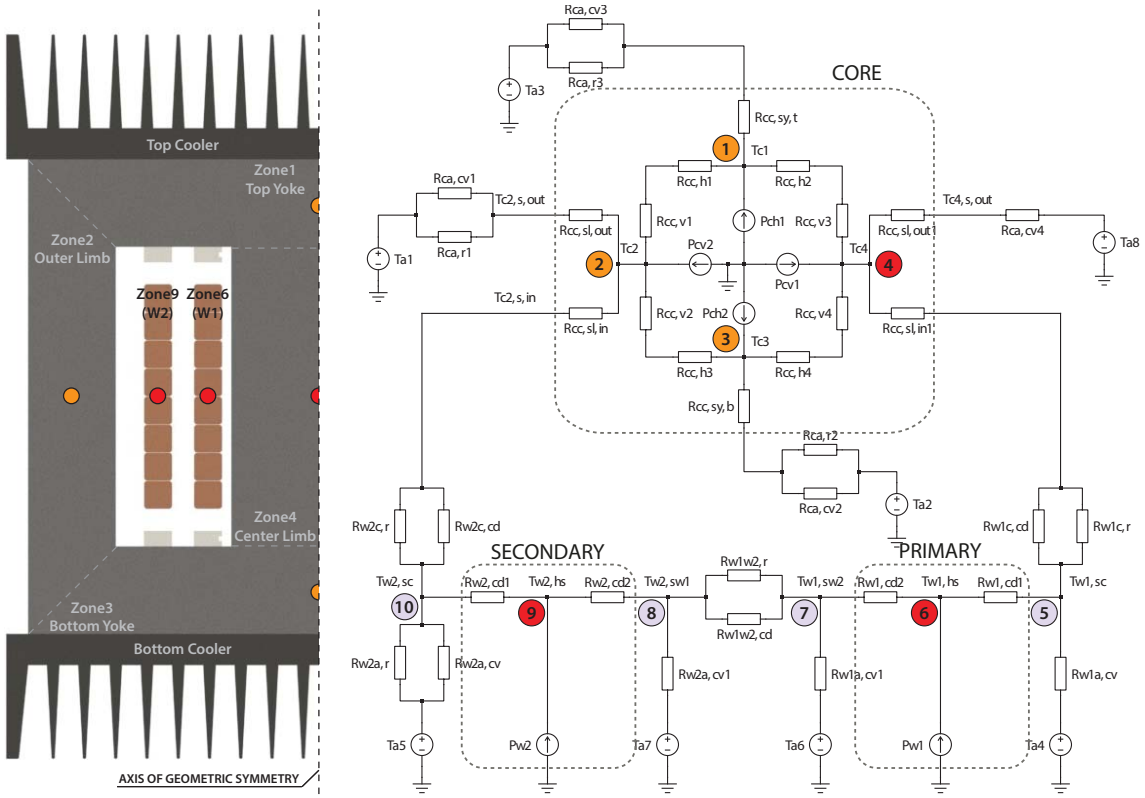

(a) (b)

Fig. 4: (a) Partitioning of the MFT into zones for thermal modeling with respect to geometric symmetry; (b) Detailed static thermal network model of the MFT based on conduction, convection and radiation thermal resistances (nodes without heat injection - gray, expected hot-spot nodes for the given design - red);

 ISBN: 9789075815269 and CFP17850-USB

The admittance matrix of this network is derived and used for efficient calculation of the temperatures at all nodes according to the injected power of losses in the windings and the core. For the given network, displayed in Fig. 4b, calculation of the temperatures in all nodes corresponds to the inversion of a (10x10) matrix, as shown in (2). Even though this seems like a low computational effort, when it comes to optimization, such as presented in Fig. 2, with polynomial complexity, decreasing the weight of the function primitives, containing the models, becomes paramount in order to enable the largest possible set of design variables and design range with reasonable discretization.

$$\mathbf{Q}_{(n)} = \mathbf{Y}_{\mathbf{th}_{(n\mathrm{x}n)}} \Delta\mathbf{T}_{(n)} \tag{2}$$

However, it is possible to rearrange the set of thermal equations displayed in (2), by bisecting the set of nodes to those that have non-zero heat power injection and those that have zero heat power injection, as shown in (3).

$$\begin{bmatrix} \mathbf{Q}_{\mathbf{A}_{(m)}} \\ \mathbf{0}_{(p)} \end{bmatrix} = \begin{bmatrix} \mathbf{Y}_{\mathbf{thAA}_{(m\mathrm{x}m)}} & \mathbf{Y}_{\mathbf{thAB}_{(m\mathrm{x}p)}} \\ \mathbf{Y}_{\mathbf{thBA}_{(p\mathrm{x}m)}} & \mathbf{Y}_{\mathbf{thBB}_{(p\mathrm{x}p)}} \end{bmatrix} \begin{bmatrix} \Delta\mathbf{T}_{\mathbf{A}_{(m)}} \\ \Delta\mathbf{T}_{\mathbf{B}_{(p)}} \end{bmatrix} \tag{3}$$

It is possible to apply the Kron reduction to (3), as shown in (4), thus reducing the matrix dimension to the number of nodes with heat injection. The result of this reduction is a reduced size Kron matrix, as given in (4), which allows calculation of the temperatures at expected hot-spot points (e.g. center of the windings and cores) according to the injected power of losses in the windings and the core.

$$\Delta\mathbf{T}_{\mathbf{A}_{(m)}} = \left(\mathbf{Y}_{\mathbf{thAA}_{(m\mathrm{x}m)}} - \mathbf{Y}_{\mathbf{thAB}_{(m\mathrm{x}p)}} \mathbf{Y}^{-1}_{\mathbf{thBB}_{(p\mathrm{x}p)}} \mathbf{Y}_{\mathbf{thBA}_{(p\mathrm{x}m)}}\right)^{-1} \mathbf{Q}_{\mathbf{A}_{(m)}} = \mathbf{Y}^{-1}_{\mathbf{Kron}_{(m\mathrm{x}m)}} \mathbf{Q}_{\mathbf{A}_{(m)}} \tag{4}$$

Thermal FEM Analysis

A detailed 2D and 3D FEM analysis is performed in order to verify the validity of the assumptions made while deriving the analytical model and its hot-spot temperature estimations, as shown in Fig. 5. The two 2D simulations, displayed in Figs. 5a and 5b, show the impact of the different cooling conditions on the temperature distribution and hot-spot magnitude of the two symmetry details with wingdings outside and inside of the core window area, respectively. The results of the full MFT 3D simulation, taking into account the anisotropic thermal conductance of the windings (litz wire), are illustrated in Fig. 5c.

Despite the obvious maximum hot-spot temperature difference between the two 2D symmetry details, due to the very high relative thermal conductivity of the litz wire along its path (through copper) compared to the radial direction (through layers of copper and enamel coating, three orders of magnitude less than pure copper), the temperature distribution along the winding turn path is practically constant in the 3D

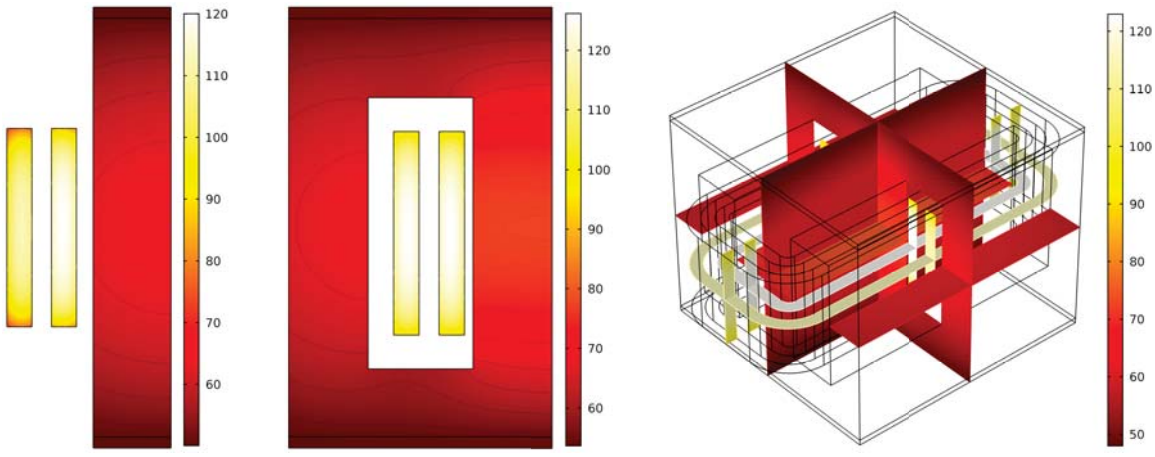

(a) (b) (c)

Fig. 5: Thermal FEM analysis of the MFT: (a) 2D symmetry detail outside of the window area, (b) 2D symmetry detail inside of the window area, (c) Full 3D model

simulation and the hot-spot magnitude is between the two 2D extreme cases. This result confirms the validity of the assumption that both cooling conditions, inside and outside of the core window area, can be taken into account analytically by putting their corresponding thermal resistances in parallel.

Finally, the analytically calculated hot-spot temperatures of the core and the windings, 74^oC and 125^oC, respectively, together with the rest of the results from Table III are very well correlated with the full 3D MFT model FEM simulation results, displayed in Fig. 5c.

Table III: Analytical thermal network MFT model temperature estimation in steady state full-load operation

$T_1\ [^oC]$	$T_2\ [^oC]$	$T_3\ [^oC]$	$T_4\ [^oC]$	$T_5\ [^oC]$	$T_6\ [^oC]$	$T_7\ [^oC]$	$T_8\ [^oC]$	$T_9\ [^oC]$	$T_{10}\ [^oC]$
51.3	59.9	58.4	73.75	114.6	124.6	116.1	110.1	116.3	104.1

MFT Prototype and test setup

An MFT prototype, as displayed in Fig. 6a, with electric specifications, as shown in Table IV, has been built based on the optimal construction specifications generated by the design optimization procedure, given in Fig. 2. It is a shell type, air-insulated and natural-air-cooled MFT, featuring AWG 32 square litz wire windings and N87 SIFERRIT U-cores. Primary and secondary winding coil-formers have been custom designed and optimized in 3D CAD to maximize the cooling surface for natural air convection on the windings [8], resulting in geometry, as illustrated in Fig. 4a.

Table IV: N87 SIFERRIT MFT prototype electric specifications

P_n	V_1	V_2	f_{sw}	L_{sp}, L_{ss}	L_m
$100kW$	$750V$	$750V$	$10kHz$	$4.2\mu H$	$750\mu H$

A resonant test setup composed of two power converters connected in back-to-back configuration and additional DC power supplies, allowing for full power to be circulated through the MFT, has been assembled. The electrical scheme and physical layout of this setup within the protective cage are displayed in Fig. 6b and Fig. 7a, respectively [8]. With this setup, heat run tests can be effectively carried out, allowing for thermal equilibrium to be reached and therefore the experimental thermal characterization in steady state, considering non-negligible thermal capacity of the MFT prototype.

Temperature measurements were performed with thermocouple probes and thermal camera. The MFT was equiped with thermocouple probes at various points within the secondary winding and the core, as

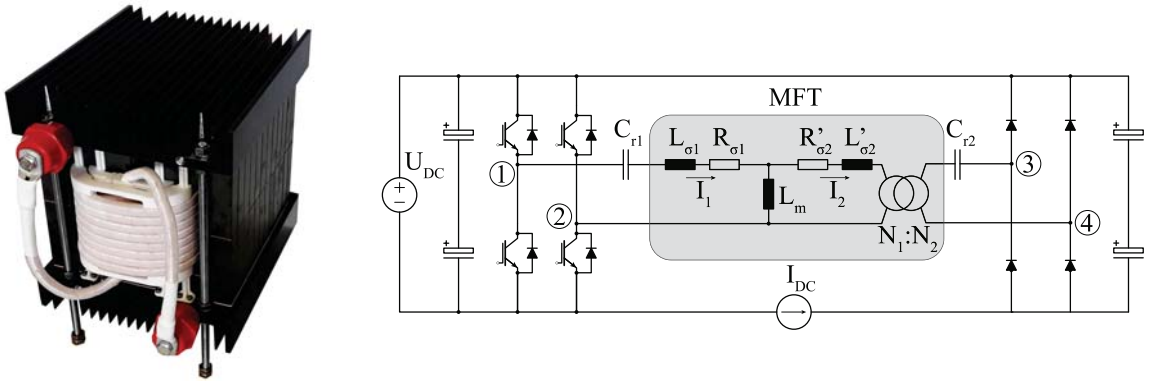

(a) (b)

Fig. 6: (a) MFT prototype based on the optimal design; (b) Electrical scheme of the resonant test setup capable of circulating $100kW$ through the MFT;

(a) (b)

Fig. 7: (a) Resonant test setup within the protective cage; (b) MFT equipped with thermal probes;

illustrated in Fig. 7b. All temperature measurements were synced to the PC in real time via wireless transmitters during thermal runs enabling both apropriate monitoring and documenting of the measured temperatures for post processing. A priori to the thermal run, the thermal camera was properly calibrated to different surface emissivities of different MFT surfaces.

Experimental Validation

The thermal run test is designed to achieve two different steady states of the MFT, namely no-load and full-load operation. Besides the verification of the hot-spot temperature estimations, this allows to expose the influence of the coupling thermal resistances between the windings and the core. Electrical measurements of the characteristic resonant waveforms on the primary side of the resonant tank, in the two mentioned steady states, are displayed in Fig. 8 indicating correct resonant converter operation.

The thermal measurements of the thermocouple probes over the nine-hour thermal run and thermal camera images in the no-load and full-load steady state operation are shown in Fig. 9. Thermal measurements show the hot-spot temperatures of the core and the windings in the two corresponding steady states as well as the dynamics of the system, namely the two different thermal time constants of the core and the windings. In the no-load operation, winding losses are negligible (limited to only the magnetization

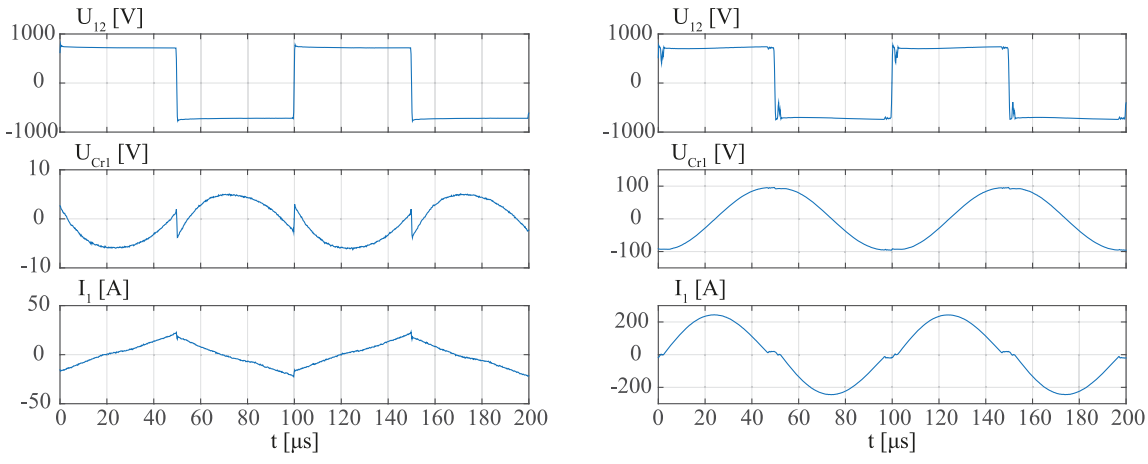

(a) (b)

Fig. 8: Resonant converter voltage waveform on primary side of the resonant tank (top plot), voltage waveform on primary side resonant capacitor (middle plot), primary side resonant current in no-load (a) and full-load (b) operation

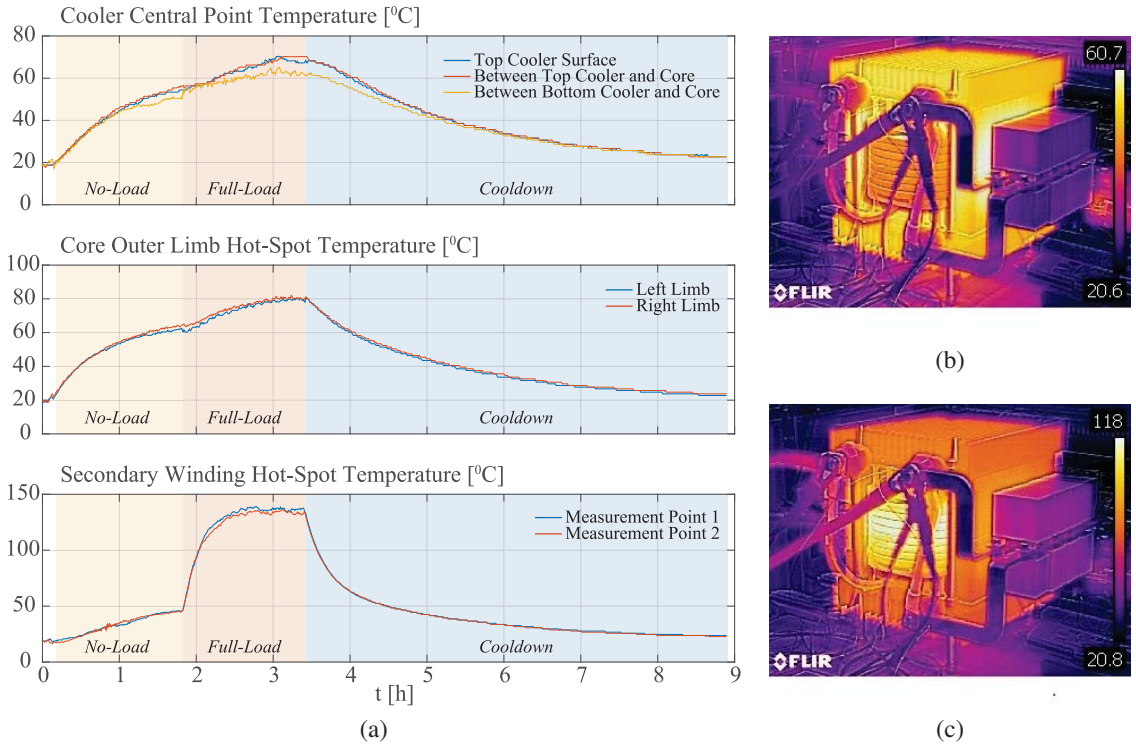

Fig. 9: (a) Measurements on thermocouple probes during the nine-hour thermal run; (b) Thermal camera image in the no-load steady state; (c) Thermal camera image in the full-load steady state;

current in the primary winding) and the MFT is heating up only due to the nominal core losses. Therefore, it can be seen that the core temperature is higher than the winding temperature, which are receiving heat through the coupling thermal resistances. On the other hand, in the full load condition, MFT is heating up due to both the core and the winding nominal losses and the winding temperature is higher than the core temperature according to the design.

However, due to the low accuracy of the used empirical formulas for natural air convection, the temperature rise of the MFT measurement points was slightly higher than predicted. These formulas are developed for the case of a hot rectangular plate in free space which is obviously not the same as the geometry of the MFT. Consequently, the influence of the reduced air flow conditions within the core window area due to the physical barriers, core and coil former structures, are neglected. This conclusion is also supported by the fact that the analytical model results correlate very well with the 3D FEM simulations, where the same empirical convection formulas were used to define convection boundary conditions.

Accuracy of the thermal model can be improved by developing sophisticated custom made natural convection formulas, as they represent the biggest hindrance. However, it is also interesting to mention that the convective thermal resistances are much more accurately predicted in case of forced cooling with defined fluid flow, and the accuracy of the whole model is expected to be much better in case of these types of designs.

Conclusion

The MFT design optimization is a rather complex process, involving various multi-physics domain couplings that must be simultaneously taken into account. Thermal modeling of the MFT is a principal element of any design optimization, where simple and sufficiently accurate analytical models are required to speed up the process, in contrast to detailed and computationally intensive FEM models, useful for final design verification.

A detailed analytical steady-state thermal network MFT model has been presented and verified via FEM analysis and experimentally. A very good correlation between the analytical and FEM model results,

utilizing the same natural convection formulas, indicates that the developed model is very accurate. However, due to the low quality of the empirical natural air convection models and their limited applicability on the given geometry details, the measured temperatures were slightly higher than the estimated ones. For those reasons, analytical models, while fast to execute, have to be carefully correlated with experimental measurements.

Finally, the presented model is generic, and can easily be applied to any different MFT type (e.g. core-type or C-type, different core and winding materials, different cooling methods and media) by simple adjustment of the values of the corresponding coupling thermal resistances between the MFT partitions from Fig. 4a, according to the selected design choices.

References

[1] M. Claessens et al. "Traction Transformation: A Power-Electronic Traction Transformer (PETT)". In: *ABB Review, No: 1/12* (2012), pp. 11–17.

[2] J. E. Huber and J. W. Kolar. "Solid-State Transformers: On the Origins and Evolution of Key Concepts". In: *IEEE Ind. Electron. Mag.* 10.3 (Sept. 2016), pp. 19–28.

[3] A. Van den Bossche and V. C. Valchev. *Inductors and Transformers for Power Electronics*. Taylor & Francis, Mar. 2005. ISBN: 978-1-4200-2728-0.

[4] K. Ilves. "Thermal Modeling of a Medium Frequency Transformer". MSc Thesis. KTH, Stockholm, Sweden, 2009.

[5] I. Villar. "Multiphysical Characterization of Medium-Frequency Power Electronic Transformers". PhD thesis. EPFL Lausanne, Switzerland, 2010.

[6] G. Ortiz. "High-Power DC-DC Converter Technologies for Smart Grid and Traction Applications". PhD thesis. ETH Zurich, Switzerland, 2014.

[7] M. Bahmani. "Design and Optimization Considerations of Medium-Frequency Power Transformers in High-Power DC-DC Applications". PhD thesis. Chalmers University of Technology Gothenburg, Sweden, 2016.

[8] M. Mogorovic and D. Dujic. "Medium Frequency Transformer Design and Optimization". In: *Power Conversion and Intelligent Motion - (PCIM) 2017*. Nuremberg, Germany, 2017., pp. 423–430.

[9] *Convection From a Rectangular Plate*. http://people.csail.mit.edu/jaffer/SimRoof/Convection/.

[10] F. M. White. *Viscous Fluid Flow*. McGraw-Hill Higher Education, 2006. ISBN: 978-0-07-124493-0.

[11] K. Venkatachalam et al. "Accurate Prediction of Ferrite Core Loss with Nonsinusoidal Waveforms Using Only Steinmetz Parameters". In: *Proc. of IEEE Workshop on Computers in Power Electronics*. June 2002, pp. 36–41.

[12] P. L. Dowell. "Effects of Eddy Currents in Transformer Windings". In: *Proc. of the Institution of Electrical Engineers* 113.8 (Aug. 1966), pp. 1387–1394.